Chemical Papers
https://doi.org/10.1007/s11696-023-02854-9

ORIGINAL PAPER

Mössbauer study of thermal behavior of CL20ES and CL50WS steel powders used in selective laser melting

Tatiana Ivanova[1] · Michal Kořenek[1] · Miroslav Mashlan[1] · Veronika Svačinová[1]

Received: 21 December 2022 / Accepted: 2 May 2023

Abstract

The phase and structural changes of steel powders CL20ES and CL50WS used in additive manufacturing were studied by Mössbauer spectroscopy and X-ray diffraction. Investigated powders were annealed in the temperature range 500 °C–1100 °C in oxidizing and inert atmosphere. Annealing in an oxidizing atmosphere resulted in the formation of different iron oxides in both steel powders depending on the annealing temperature. In addition, a phase change of ferrite to austenite was identified when annealing CL50WS steel powder in an oxidizing atmosphere. This phase change was confirmed by annealing given CL50WS steel powder in an inert nitrogen atmosphere. The transformation of austenite to ferrite phase was observed only, when annealing CL20ES steel powder in an inert atmosphere at 1100 °C. Morphological changes on the surface of the spherical powders were observed by scanning electron microscopy.

Keywords Stainless 1.4404 · Maraging 1.2709 · Selective laser melting · Ferrite · Austenite · Iron oxide · Mössbauer spectroscopy · Scanning electron microscopy · X-ray diffraction

Introduction

Powders of the stainless steel 1.4404 (CL20ES) and maraging steel 1.2709 (CL50WS) are used in additive manufacturing by selective laser melting (SLM). Metal powders of these classes are among the most common metal powders for SLM (Lu et al. 2015). One of the main properties of stainless steels is their high corrosion resistance, which ensures their use in many areas of industry (petroleum, nuclear, chemical, etc.) (Guan et al. 2013; Yang et al. 2019). The combination of high strength and thermal properties makes maraging steels a promising material (Gerov et al. 2022; Kang et al. 2018). In previous studies (Mashlan et al. 2019; Linderhof et al. 2021), changes in the phase composition of parts made of CL50WS steel powder were identified. The phase transformation "austenite to martensite" was observed as a consequence of the SLM process itself. The inverse transformation was observed during the subsequent annealing of parts made by SLM. Oxidation of the surface of parts made of both steel powders (CL50WS and CL20ES) during their annealing in an air atmosphere was observed also in (Linderhof et al. (2021); Sedláčková et al. 2022; Ivanova et al. 2022). Phase changes and oxidation during annealing of various types of stainless and structural steels have been identified by other authors (Bautista et al. 2003; Salman et al. 2019; Saeidi et al. 2015; Zhou et al. 2020). The effect of annealing on the microstructure (metallographic analysis) and mechanical behaviors of parts made of 316L steel by the SLM was investigated (Zeng et al. 2021; Chao et al. 2021; Lei et al. 2021). Structural and phase transformations of Cr-Ni stainless steel powder for SLM were studied in Barabaszová et al. (2022).

In order to trace how the annealing temperature and atmosphere affect the samples under study, stainless steel metal powder (CL20ES) and maraging (CL50WS) metal powder were annealed in the temperature range of 500–1100 °C in oxidizing and inert atmospheres. Phase and structural changes of annealed samples were studied by transmission Mössbauer spectroscopy (TMS) and X-ray powder diffraction (XRD). Morphological changes on the surface of the spherical powders were observed by scanning

This work was presented at the European Symposium on Analytical Spectrometry ESAS 2022 & 17th Czech-Slovak Spectroscopic Conference held in Brno, Czech Republic on September 4–9, 2022.

✉ Tatiana Ivanova
tatiana.ivanova01@upol.cz

[1] Faculty of Science, Palacký University, 17. Listopadu 1192/12, 77900 Olomouc, Czech Republic

Published online: 15 May 2023

electron microscopy (SEM). The distribution of elements on the surface of spherical powders was monitored by energy-dispersive X-ray spectroscopy (EDS).

Materials and methods

CL50WS and CL20ES steel powders and sample preparation

CL20ES and CL50WS steel powders with their chemical composition presented in Table 1 were annealed in the temperature range of 500–1100 °C with a step of 100 °C in air and a nitrogen atmosphere for one hour. The original particles of CL20ES and CL50WS steel powders have spherical form, Figs. 2 and 3 in Linderhof et al. (2021). Air annealing was performed in a laboratory furnace (LE05/11, LAC, Zidlochovice, Czech Republic). The initial steel powder was always placed in a furnace heated to the required temperature. The sample was removed from the oven after one hour. The samples cooled spontaneously outside the furnace. Annealing in a nitrogen atmosphere was performed in a laboratory furnace with rotary reactor HTR 11/75 1100 °C. The initial powder was placed in a cooling oven, where the required temperature was subsequently reached at a rate of 40 °C/min. At this temperature, the sample was annealed for one hour and then spontaneously cooled in an oven until room temperature was reached.

Mössbauer spectroscopy

The transmission ^{57}Fe Mössbauer spectra were accumulated by a Mössbauer spectrometer operating in constant acceleration mode and equipped with a ^{57}Co(Rh) source and MS96 Mössbauer spectrometer software (Pechousek and Mashlan 2005) at room temperature. Spectra were recorded on 512 channels. The YAP:CE scintillation detector (Fyodorov et al. 1994) registering 14.4 keV γ-rays was used for the spectra accumulation. The least squares fit of the lines using the MossWinn 4.0 software program (Klencsar et al. 1996, 1998) performed the calculation and evaluation of the Mössbauer spectra. The isomer shift values were referred to the centroid of the spectrum recorded from an α-Fe foil (thickness 30 μm) at room temperature.

X-ray diffraction

All XRD measurements were taken on an X-ray diffractometer Bruker Advance D8 (Bruker, Billerica, MA, USA) equipped with a Co K_α X-ray source and LYNXEYE position-sensitive detector. The diffractometer works with Bragg–Brentano parafocusing geometry. Current and voltage values for the X-ray tube were 40 mA and 35 kV, respectively. Measurements were taken in the 2θ range of 20°–130° with step 0.02° and time per step 3.00 s. The diffractometer was equipped with a 0.6-mm divergence slit and 2.5° axial Soller slits for the primary beam path and 20-μm Fe K_β filter and 2.5° axial Soller slits for the secondary beam path.

Scanning electron microscopy

The VEGA3 LMU (TESCAN, Brno, Czech Republic) scanning electron microscope was chosen to study the surface morphology and elemental composition using energy-dispersive X-ray spectroscopy. The electron source in this microscope is the LaB_6 cathode. The microscope includes two detectors: a secondary electron detector of the Everhart–Thornley type (TESCAN, Brno, Czech Republic) and an XFlash silicon drift detector 410-M (Bruker Nano GmbH, Berlin, Germany).

Results and discussion

Annealing of CL20ES powder in an oxidizing atmosphere

The transmission Mössbauer spectra of the CL20ES annealed powder are shown in Fig. 1. A single peak of CL20ES metal powder, which is present in all (annealed and unannealed) samples, is characteristic of γ-austenite phase (FCC structure). In fact, the single peak is characteristic for the pure γ-Fe (FCC structure) Mössbauer spectrum, but substitutional and interstitial atoms (dominantly Cr and Ni) cause a broadening of the spectrum; therefore, the Mössbauer spectrum is fitted with a doublet with small-quadrupole splitting (Cook 1987) (Table 2). In samples annealed at a temperature of 700 °C and higher, a typical sextet α-Fe_2O_3 (hematite) (Zboril et al. 2002)

Table 1 Chemical composition of the metal powders (material data Concept Laser GmbH)

Steel powder	Element concentration, wt %										
	Fe	C	Si	Mn	P	S	Cr	Mo	Ni	Ti	Co
CL20ES	Balance	≤0.03	0–1.0	0–2.0	≤0.045	≤0.03	16.5–18.5	2.0–2.5	10.0–13.0	–	–
CL50WS	Balance	≤0.03	≤0.1	≤0.15	≤0.01	≤0.01	≤0.025	4.5–5.2	17.0–19.0	0.80–1.20	8.50–10.0

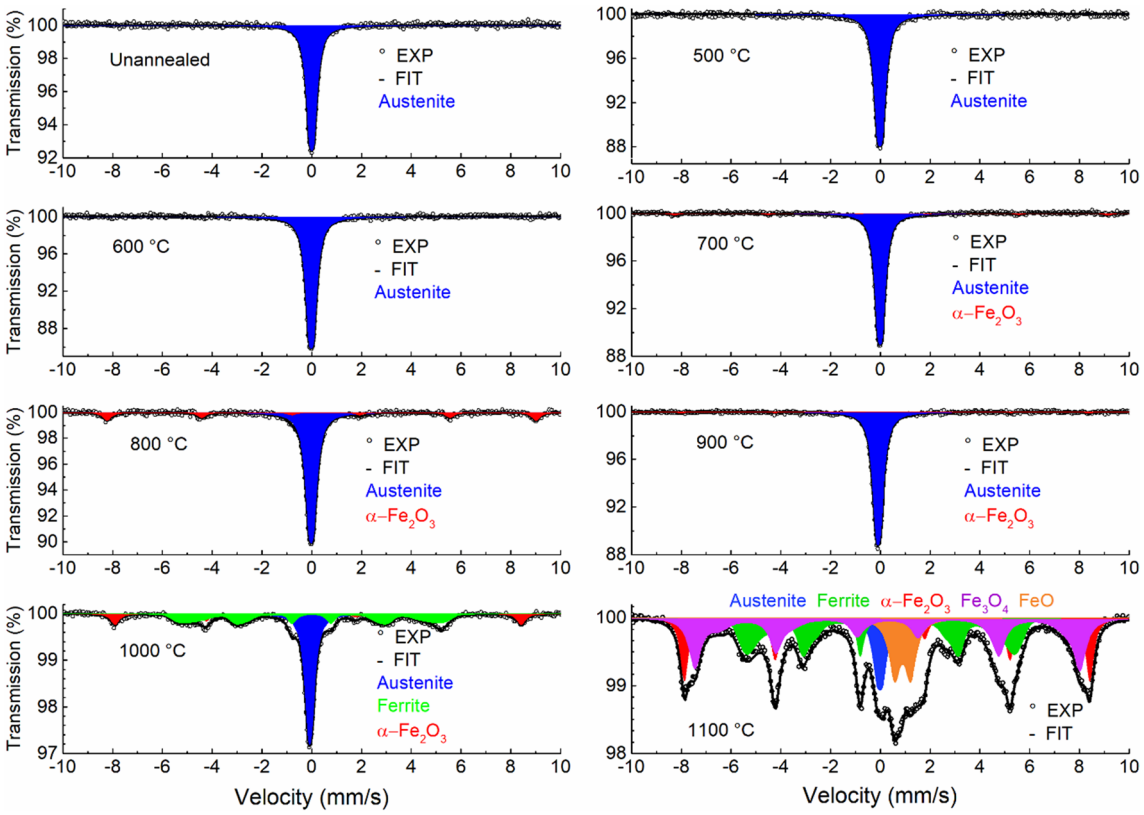

Fig. 1 Mössbauer spectra of annealed CL20ES powder in the oxidizing atmosphere

Table 2 Mössbauer parameters of annealed CL20ES powder in the oxidizing atmosphere (IS—isomer shift, QS/ε—quadrupole splitting/shift, FWHM—full width at half maximum, B—hyperfine magnetic field, A—spectrum area)

Temperature	Phase	IS (mm/s)	QS/ε (mm/s)	FWHM (mm/s)	B (T)	A (%)
Unannealed	FCC austenite	−0.06 ± 0.01	0.16 ± 0.02	0.34 ± 0.02	–	100
500 °C	FCC austenite	−0.09 ± 0.01	0.20 ± 0.01	0.36 ± 0.01	–	100
600 °C	FCC austenite	−0.10 ± 0.01	0.20 ± 0.01	0.35 ± 0.01	–	100
700 °C	FCC austenite	−0.10 ± 0.01	0.18 ± 0.01	0.32 ± 0.01	–	96 ± 2
	α-Fe_2O_3	0.36 ± 0.03	−0.08 ± 0.05	0.32 ± 0.07	51.4 ± 0.5	4 ± 2
800 °C	FCC austenite	−0.10 ± 0.01	0.19 ± 0.01	0.35 ± 0.01	–	83 ± 2
	α-Fe_2O_3	0.38 ± 0.01	−0.17 ± 0.02	0.37 ± 0.03	51.3 ± 0.5	17 ± 2
900 °C	FCC austenite	−0.09 ± 0.01	0.19 ± 0.01	0.36 ± 0.01	–	98 ± 2
	α-Fe_2O_3	0.35 ± 0.05	−0.31 ± 0.10	0.35*	50.9 ± 0.5	2 ± 2
1000 °C	FCC austenite	−0.08 ± 0.01	0.15 ± 0.01	0.37 ± 0.01	–	48 ± 2
	BCC ferrite	0.00 ± 0.02	–	0.28 ± 0.02	29.8#	36 ± 2
	α-Fe_2O_3	0.37 ± 0.05	−0.22 ± 0.02	0.42 ± 0.05	50.7 ± 0.5	16 ± 2
1100 °C	FCC austenite	−0.06 ± 0.02	0.24 ± 0.02	0.43 ± 0.02	–	8 ± 2
	BCC ferrite	0.02 ± 0.01	–	0.21 ± 0.02	30.4#	26 ± 2
	α-Fe_2O_3	0.38 ± 0.01	−0.22 ± 0.01	0.39 ± 0.02	50.6 ± 0.5	19 ± 2
	T-Fe_3O_4	0.28 ± 0.01	–	0.59 ± 0.03	48.1 ± 0.5	22 ± 2
	O-Fe_3O_4	0.49 ± 0.03	–	1.05 ± 0.14	43.2 ± 0.5	8 ± 2
	wüstite	0.90 ± 0.01	0.63 ± 0.02	0.55 ± 0.01	–	12 ± 2
	Fe^{2+} doublet	1.08 ± 0.02	1.18 ± 0.03	0.50 ± 0.03	–	5 ± 2

*fixed parameter, #magnetic field distribution

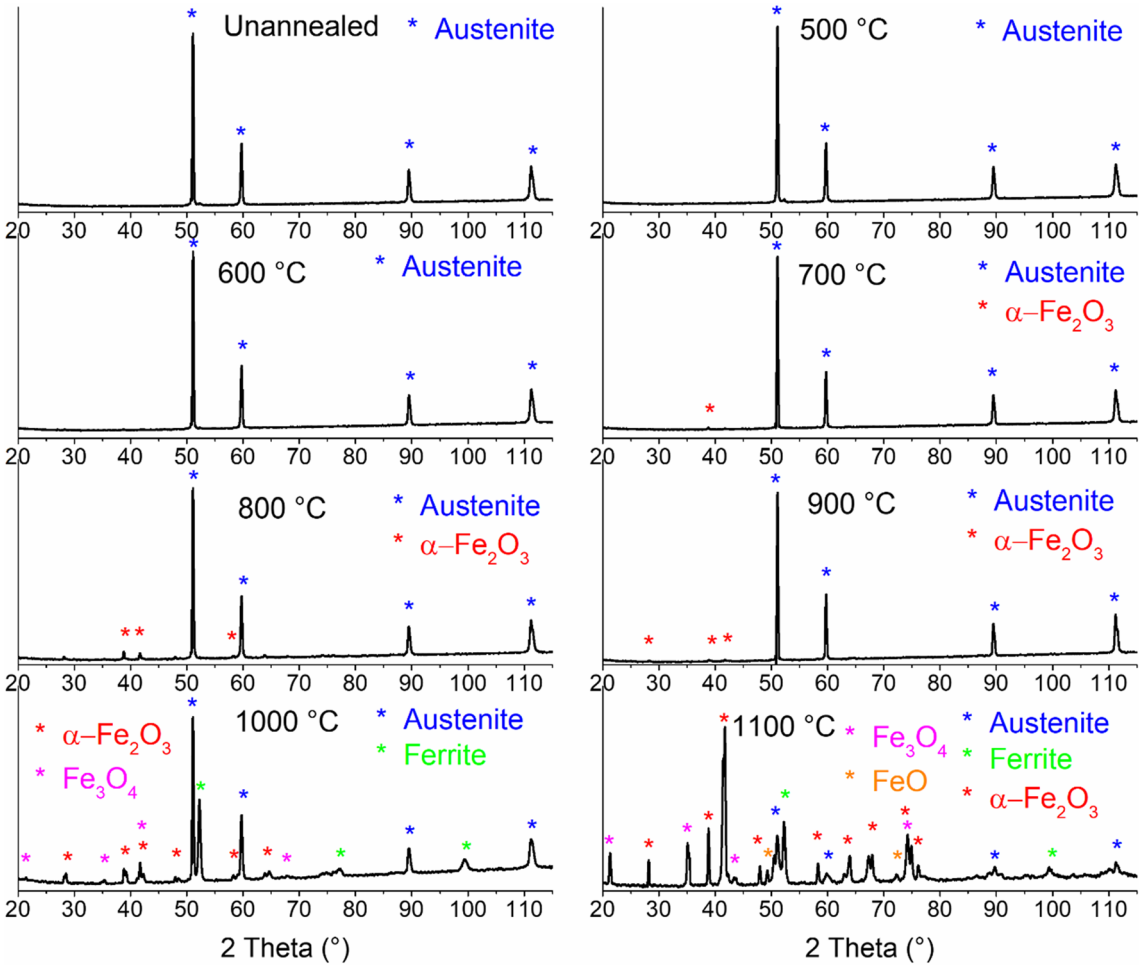

Fig. 2 X-ray powder diffraction patterns of annealed CL20ES powder in the oxidizing atmosphere

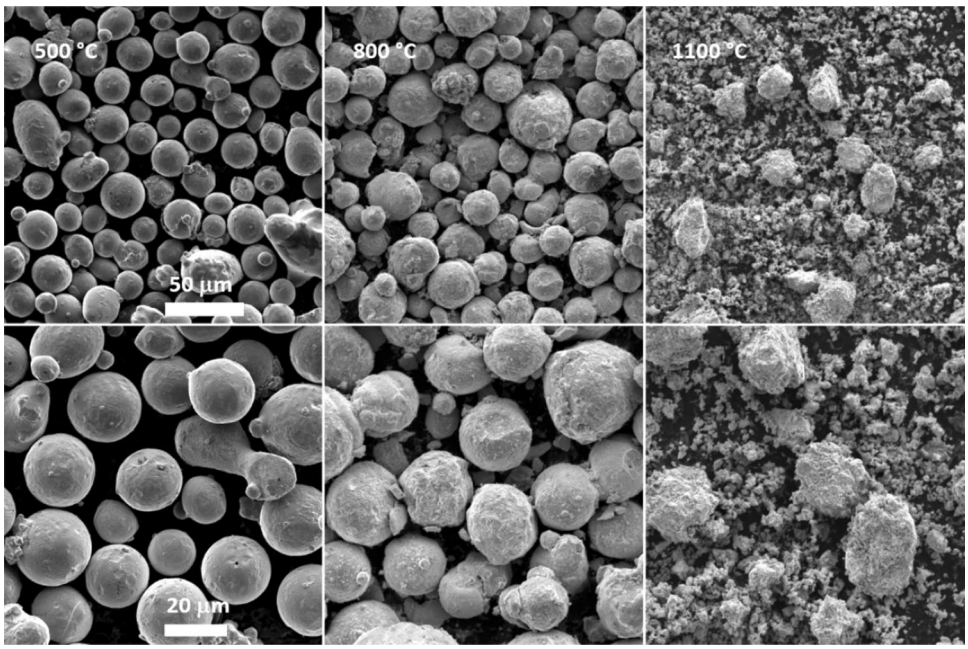

Fig. 3 Scanning electron microscopy images of annealed CL20ES powder in the oxidizing atmosphere

appears and its contribution gradually increases with temperature. The exception is the decrease in α-Fe_2O_3 content at the annealing temperature of 900 °C; this decrease may be related to the beginning of the transformation of the austenitic phase into the ferritic one. The onset of this transformation was fully manifested only in the sample annealed at a temperature of 1000 °C. The austenitic phase transformation to the ferritic phase continues more intensively even at a temperature of 1100 °C. At the same time, the oxidation process continues, but this takes place predominantly with the formation of Fe_3O_4 (magnetite) and even FeO (wüstite) (Zboril et al. 2002). The transformation of the austenitic phase into the ferritic phase as well as the formation of all oxidation products was confirmed by XRD (Fig. 2). The dominance of oxidation to magnetite and wüstite at a temperature of 1100 °C may be related to impaired access to oxygen. The surface of the particles is primarily covered with a layer of hematite, which prevents the access of oxygen and the oxidation of iron is not complete. The emergence of a certain surface layer is demonstrated by images from an electron microscope (Fig. 3), where we see that the particles before the definitive disintegration are covered by a certain layer.

Annealing of CL50WS powder in oxidizing atmosphere

In the case of annealing the CL50WS metal powder, TMS indicates gradual oxidation of the powder (Fig. 4). The degree of oxidation increases with temperature, and different types of iron oxides have been identified. The α-Fe_2O_3, which appears already from annealing at 500 °C, and Fe_3O_4, which appears at 600 °C, were gradually identified. At temperatures higher than 900 °C, FeO (wüstite) was identified. At the same time, Mössbauer spectra show that at temperatures of 600 and 700 °C, the transformation of the ferritic phase into the austenitic phase occurs. Both the oxidation processes and the transformation of the ferritic phase to austenitic are confirmed by XRD (Fig. 5). The fitting results and all hyperfine parameters for CL50WS samples annealed at the oxidized atmosphere are presented in Table 3. In the Mössbauer spectrum of a sample annealed at a temperature of 1100 °C the presence of Fe^{2+} doublet can be seen. Based on the principles of Mössbauer spectroscopy, it can be assumed that the registered phase is an iron-containing oxide. The majority amount of alloying elements in the original maraging steel powder accounted for nickel and cobalt (Table 1). In the oxidizing atmosphere, the maraging steel metal powder is prone to the formation of spinel $CoFe_2O_4$

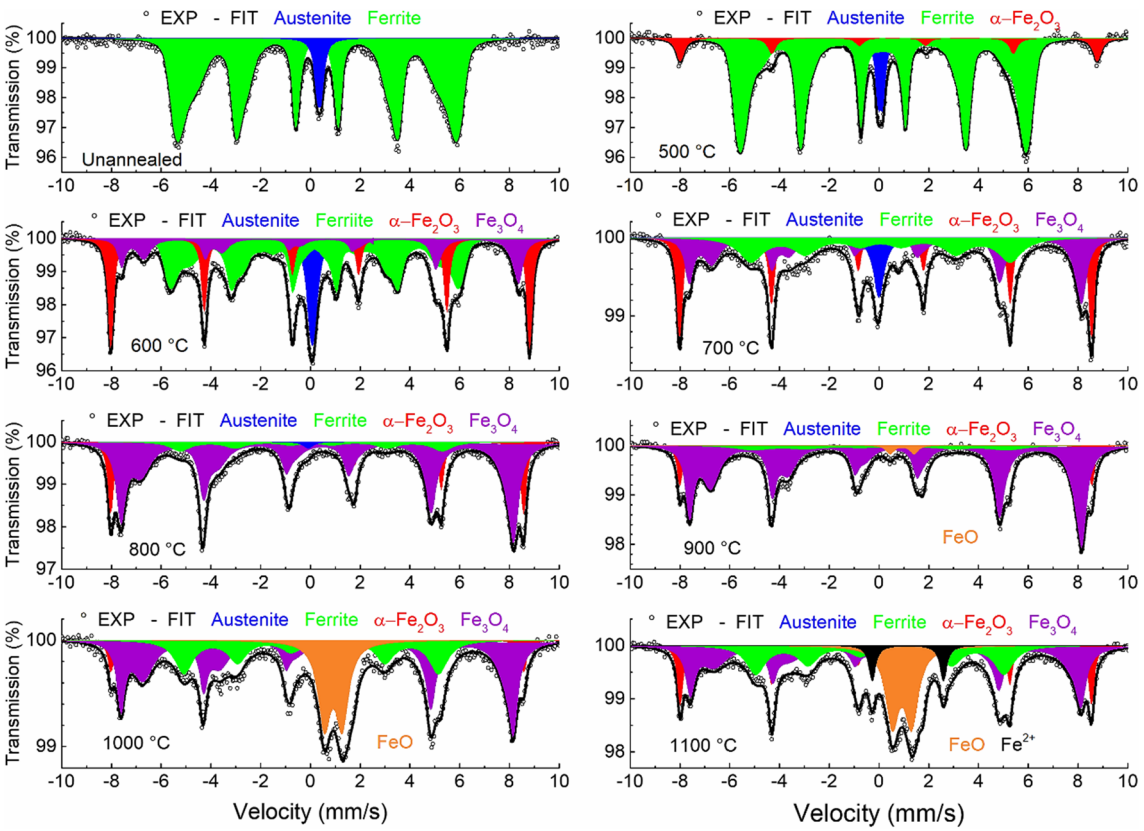

Fig. 4 Mössbauer spectra of annealed CL50WS powder in the oxidizing atmosphere

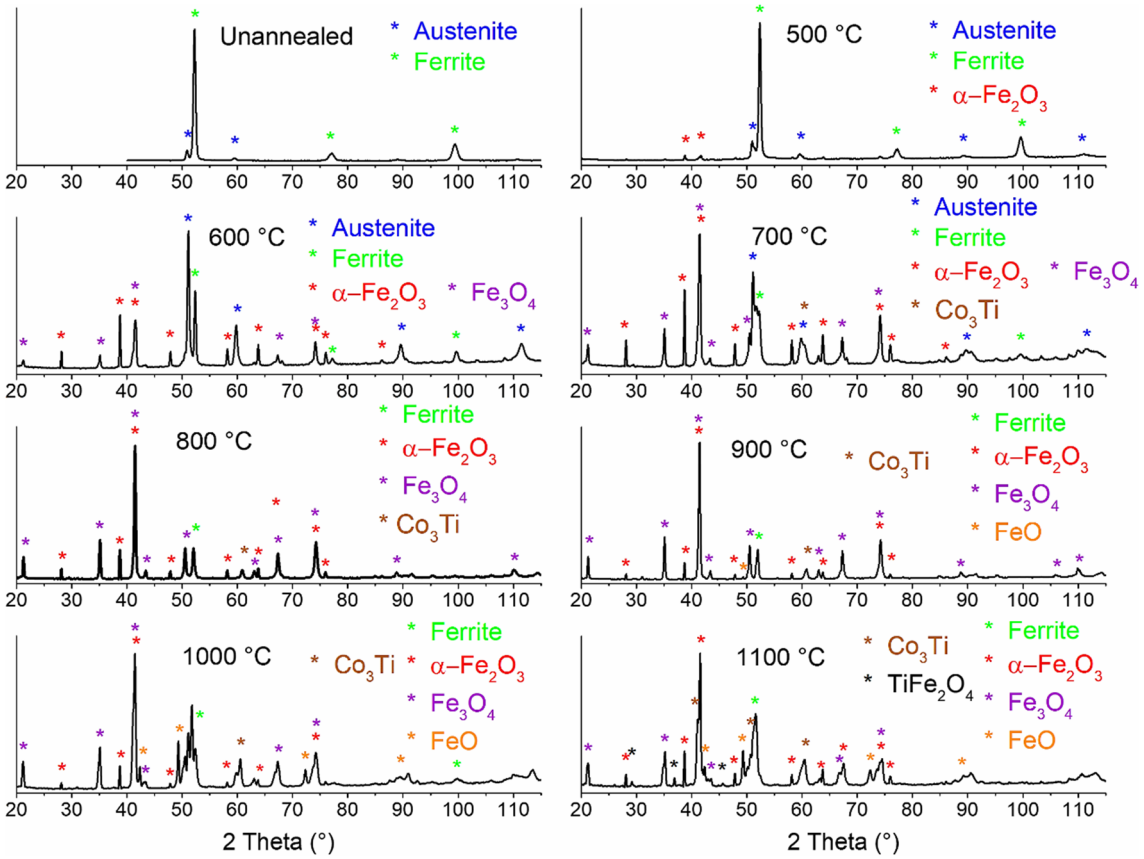

Fig. 5 X-ray diffraction patterns of annealed CL50WS powder in the oxidizing atmosphere

and $NiFe_2O_4$ (Florez et al. 2021). Both of these ferrites were studied by Mössbauer spectroscopy, which, together with magnetic measurements, points to their magnetic arrangement at room temperature, par-example (Chinnasamy et al. 2001; Kurikka et al. 1998; Ahlawat et al. 2011). Their Mössbauer spectra represent sextets. A Fe^{2+} doublet was identified by us in the Mössbauer spectrum, indicating a paramagnetic or diamagnetic arrangement. Spinels $TiFe_2O_4$ and $MoFe_2O_4$ are described in the literature (Roy et al. 2000; Wang et al. 2000; Cristobal et al. 2008; Mudarra Navarro et al. 2019), whose Mössbauer spectra consist of doublets with parameters corresponding to Fe^{2+}. Mo and Ti are other alloying elements of CL50WS steel powder whose content is greater than 1%. Based on literature research, from the point of view of Mössbauer spectroscopy, the Fe^{2+} doublet identified in the sample annealed at 1100 °C in an oxidizing atmosphere (Fig. 4, black doublet) can be attributed to mixed (Mo–Ti)Fe_2O_4 spinel. Three diffraction peaks observed in the XRD pattern (Fig. 5, 1100 °C) can be attributed to $MeFe_2O_4$ spinels (Me = Ni, Co, Mo, Ti) or their solid solution. $MeFe_2O_4$ spinels have similar crystallographic parameters, and it is rather difficult to separate these two phases by XRD. The $Mo_{1-x}Ti_xFe_2O_4$ compound was studied by both XRD and Mössbauer spectroscopy (Roy et al. 2000), and the results showed that the XRD patterns are almost identical for $0 \le x \le 1$. However, differences were visible in the Mössbauer spectra, mainly in the asymmetry of the doublet. The doublet in our Mössbauer spectrum (Fig. 4, black doublet) is symmetric, and by comparing it with the results (Roy et al. 2000), we can assign it to $TiFe_2O_4$ spinel. Due to XRD, the Co_3Ti compound was identified in the samples annealed at a temperature of 700 °C and higher. This fact is apparently related to the separation of these elements from the steel during annealing (Mashlan et al. 2019).

The morphology of the particle surface of maraging steel powder is shown in Fig. 6. As you can see, the oxidation of powder particles begins at a temperature of 500 °C. At temperatures of 800 °C and 1100 °C, due to the sintering of the samples, the metal powder particles lose their globe-form shape and begin to fall apart.

Annealing of CL20ES powder in an inert nitrogen atmosphere

Transmission Mössbauer spectra for the CL20ES stainless steel metal powder annealed at the inert nitrogen atmosphere are present in Fig. 7. A single peak on the

Table 3 Mössbauer parameters of annealed CL50WS powder in the oxidizing atmosphere (IS—isomer shift, QS/ε—quadrupole splitting/shift, FWHM—full width at half maximum, B—hyperfine magnetic field, A—spectrum area)

Temperature	Phase	IS [mm/s]	QS/ε [mm/s]	FWHM [mm/s]	B [T]	A [%]
Unannealed	FCC austenite	−0.07 ± 0.01	0.16 ± 0.02	0.22 ± 0.03	–	5 ± 2
	BCC ferrite	0.03 ± 0.01	–	0.25 ± 0.01	30.9#	95 ± 2
500 °C	FCC austenite	−0.07 ± 0.01	0.18 ± 0.01	0.24 ± 0.02	–	7 ± 2
	BCC ferrite	0.04 ± 0.01	–	0.24 ± 0.01	32.4#	83 ± 2
	α-Fe_2O_3	0.33 ± 0.01	−0.14 ± 0.02	0.40 ± 0.03	51.2 ± 0.5	10 ± 2
600 °C	FCC austenite	−0.05 ± 0.01	0.15 ± 0.02	0.38 ± 0.03	–	10 ± 2
	BCC ferrite	0.04 ± 0.01	–	0.27 ± 0.02	28.9#	45 ± 2
	α-Fe_2O_3	0.36 ± 0.01	−0.21 ± 0.01	0.27 ± 0.01	51.4 ± 0.5	26 ± 2
	T-Fe_3O_4	0.27 ± 0.01	–	0.43 ± 0.03	48.8 ± 0.5	8 ± 2
	O-Fe_3O_4	0.64 ± 0.02	–	0.65 ± 0.05	45.7 ± 0.5	11 ± 2
700 °C	FCC austenite	−0.05 ± 0.01	0.17 ± 0.02	0.36 ± 0.02	–	7 ± 2
	BCC ferrite	0.03 ± 0.01	–	0.25 ± 0.03	31.1#	26 ± 2
	α-Fe_2O_3	0.37 ± 0.01	−0.21 ± 0.01	0.29 ± 0.01	51.5 ± 0.5	31 ± 2
	T-Fe_3O_4	0.27 ± 0.01	–	0.33 ± 0.03	48.8 ± 0.5	8 ± 2
	O-Fe_3O_4	0.64 ± 0.01	–	0.76 ± 0.05	45.9 ± 0.5	18 ± 2
800 °C	FCC austenite	−0.09 ± 0.05	0.17 ± 0.07	0.50 ± 0.15	–	1 ± 2
	BCC ferrite	0.03 ± 0.03	–	0.99 ± 0.08	32.7 ± 0.5	9 ± 2
	α-Fe_2O_3	0.37 ± 0.01	−0.18 ± 0.01	0.29 ± 0.01	51.6 ± 0.5	24 ± 2
	T-Fe_3O_4	0.29 ± 0.01	–	0.45 ± 0.02	49.1 ± 0.5	33 ± 2
	O-Fe_3O_4	0.58 ± 0.01	–	0.99 ± 0.04	45.9 ± 0.5	33 ± 2
900 °C	BCC ferrite	0.03 ± 0.01	–	1.83 ± 0.31	31.8 ± 0.5	10 ± 2
	α-Fe_2O_3	0.36 ± 0.01	−0.17 ± 0.01	0.28 ± 0.01	51.5 ± 0.5	15 ± 2
	T-Fe_3O_4	0.28 ± 0.01	–	0.40 ± 0.02	49.0 ± 0.5	32 ± 2
	O-Fe_3O_4	0.66 ± 0.01	–	1.01 ± 0.05	45.8 ± 0.5	41 ± 2
	FeO	0.93 ± 0.02	0.96 ± 0.05	0.62 ± 0.02	–	2 ± 2
1000 °C	BCC ferrite	0.03 ± 0.01	–	0.88 ± 0.04	31.8 ± 0.5	23 ± 2
	α-Fe_2O_3	0.37 ± 0.01	−0.19 ± 0.02	0.31 ± 0.03	51.6 ± 0.5	9 ± 2
	T-Fe_3O_4	0.28 ± 0.01	–	0.38 ± 0.02	49.1 ± 0.5	19 ± 2
	O-Fe_3O_4	0.60 ± 0.01	–	1.01 ± 0.05	45.5 ± 0.5	30 ± 2
	FeO	0.91 ± 0.02	0.72 ± 0.01	0.62 ± 0.02	–	19 ± 2
1100 °C	BCC ferrite	0.04 ± 0.01	–	0.93 ± 0.03	31.0 ± 0.5	22 ± 2
	α-Fe_2O_3	0.37 ± 0.01	−0.20 ± 0.01	0.28 ± 0.01	51.4 ± 0.5	15 ± 2
	T-Fe_3O_4	0.24 ± 0.01	–	0.44 ± 0.02	48.8 ± 0.5	17 ± 2
	O-Fe_3O_4	0.60 ± 0.02	–	1.25 ± 0.07	44.9 ± 0.5	21 ± 2
	FeO	0.92 ± 0.02	0.77 ± 0.01	0.65 ± 0.02	–	20 ± 2
	Fe^{2+} doublet	1.16 ± 0.01	2.86 ± 0.01	0.34 ± 0.02	–	5 ± 2

magnetic field distribution

Mössbauer spectra is a characteristic of γ-phase (austenite). At an annealing temperature from 500 to 1000 °C, only a doublet corresponding to the austenitic phase is observed on the spectrum. When annealing 1100 °C, in addition to the traditional austenitic phase of iron, the presence of a sextet corresponding to the ferritic phase (α-phase) (Fig. 7, red spectrum) can be seen on the spectrum. It can be concluded that the phase transformation of austenite into ferrite begins in an inert nitrogen atmosphere at a temperature of 1100 °C. The hyperfine parameters obtained using the MossWinn 4.0 software program are presented in Table 4.

The results of XRD measurements (Fig. 8) confirm the conclusions obtained using TMS. The XRD pattern obtained from a sample annealed at a temperature of 1100 °C shows the presence of an austenitic phase of iron, as well as a small peak corresponding to the ferritic phase (Fig. 8). At an annealing temperature of ≥ 900 °C, the appearance of the chromium nitride (Cr_2N) phase can be seen on the X-ray patterns. Chromium nitride (Cr_2N) has a phase prototype in the form of iron nitride (Fe_2N). Based on the principles of Mössbauer spectroscopy, only phases containing iron nuclei can be recorded. Chromium is the first alloying element in the chemical composition of

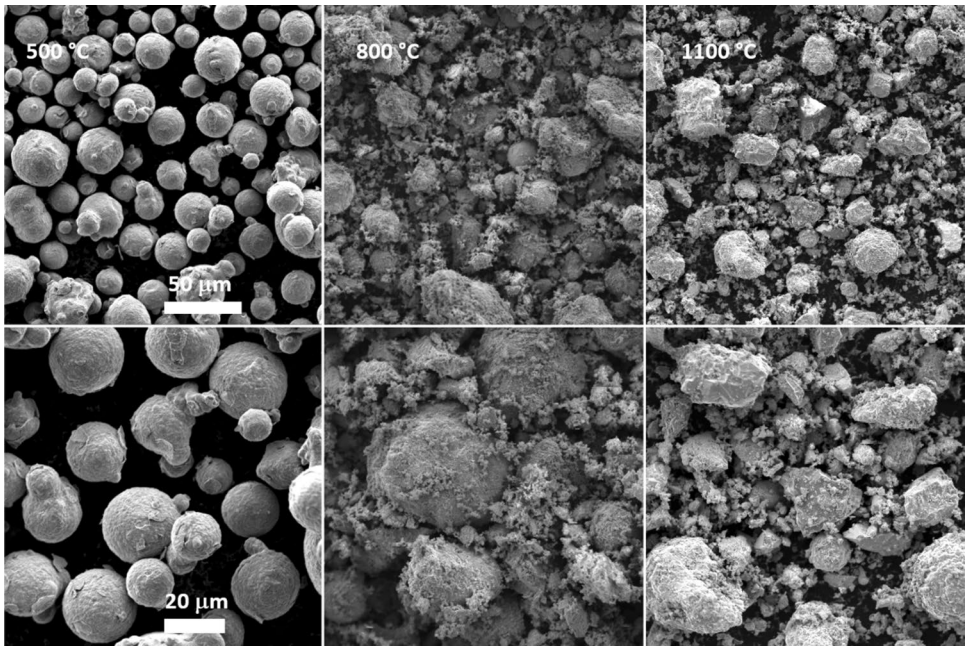

Fig. 6 Scanning electron microscopy images of annealed CL50WS powder in the oxidizing atmosphere

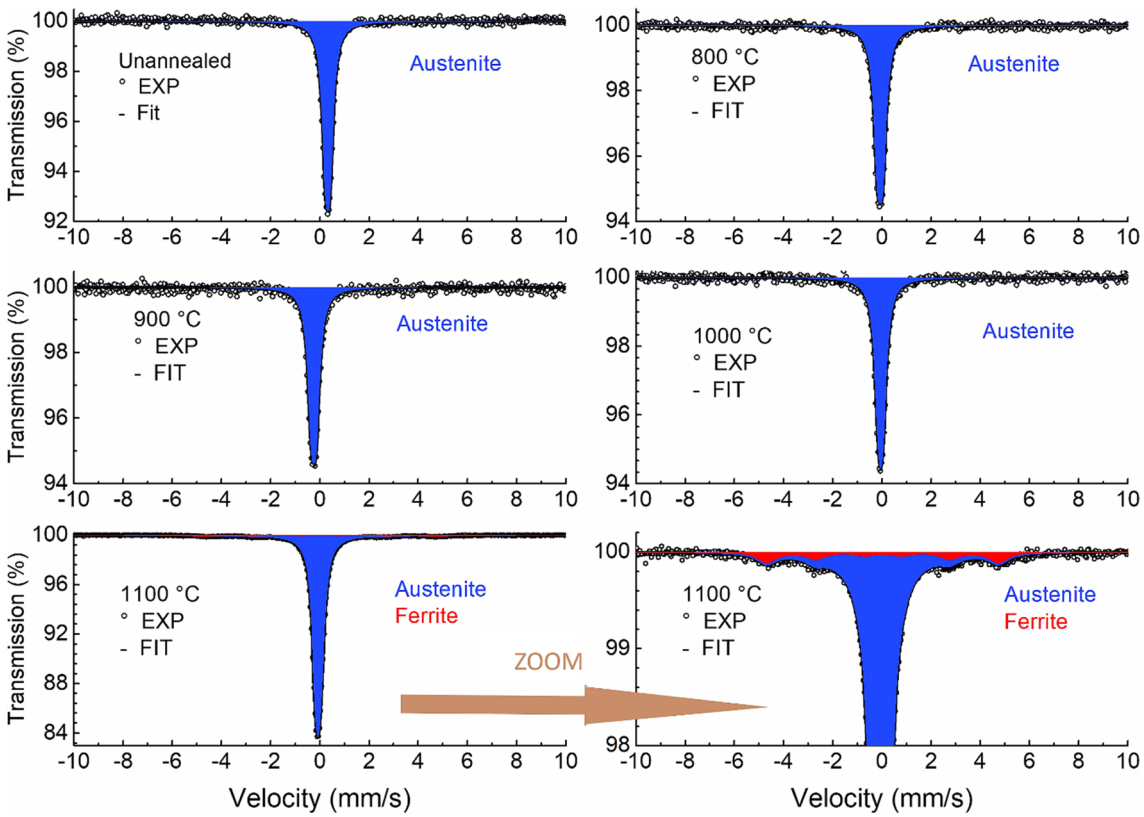

Fig. 7 Mössbauer spectra of annealed CL20ES powder in the inert nitrogen atmosphere

stainless steel (Table 1). Among all alloying elements of the initial powder material, chromium is most predisposed to diffusion under the influence of temperature than other elements (Pechousek and Mashlan 2005).

Studies of the surface morphology of the CL20ES particles using SEM are given in Fig. 9, which shows the results of measurements during annealing of 800 and 1100 °C. As can be seen, annealing in an inert nitrogen atmosphere does

Table 4 Mössbauer parameters of annealed CL20ES powder in inert nitrogen atmosphere (IS—isomer shift, QS/ε—quadrupole splitting/shift, FWHM—full width at half maximum, B—hyperfine magnetic field, A—spectrum area)

Temperature	Phase	IS (mm/s)	QS/ε (mm/s)	FWHM (mm/s)	B (T)	A (%)
Unannealed	FCC austenite	−0.06 ± 0.01	0.16 ± 0.02	0.34 ± 0.02	–	100
800 °C	FCC austenite	−0.09 ± 0.01	0.21 ± 0.01	0.36 ± 0.01	–	100
900 °C	FCC austenite	−0.08 ± 0.01	0.20 ± 0.01	0.35 ± 0.01	–	100
1000 °C	FCC austenite	−0.07 ± 0.01	0.17 ± 0.01	0.36 ± 0.01	–	100
1100 °C	FCC austenite	−0.08 ± 0.01	0.19 ± 0.01	0.35 ± 0.01	–	95 ± 2
	BCC ferrite	−0.02 ± 0.03	–	0.96 ± 0.07	29.4 ± 0.5	5 ± 2

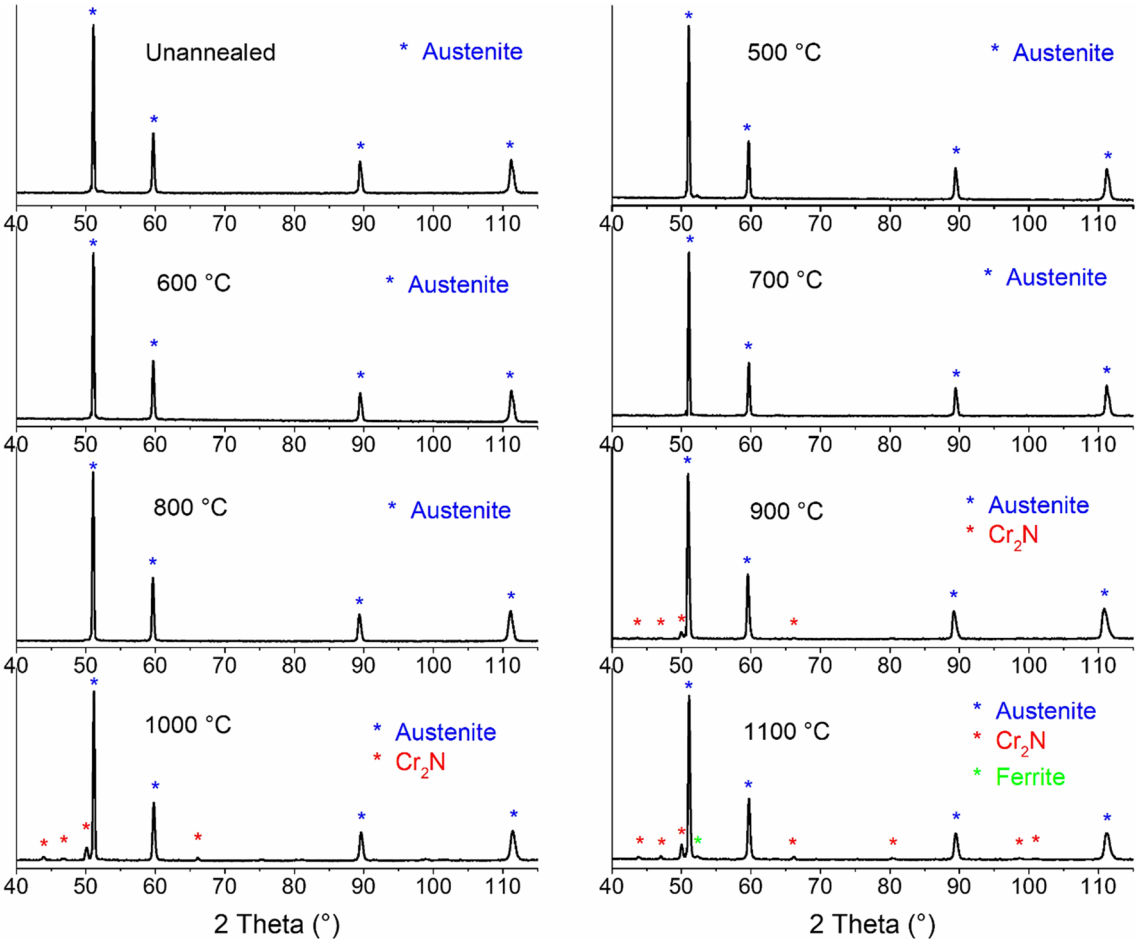

Fig. 8 X-ray powder diffraction patterns of annealed CL20ES powder in the inert nitrogen atmosphere

not lead to the sintering of metal powder. All particles of annealed metal powder have the shape of a sphere. With a more detailed magnification, it can be seen that the surfaces of the particles are more rough with an increase in the annealing temperature. In order to investigate the composition of the particle «crust», an analysis of the basic distribution of elements for the same sample was carried out (Fig. 10). Based on the results obtained, it can be concluded that the surfaces of stainless steel metal powder particles are covered with chromium pieces (Fig. 10). The chromium amount on the surface increases with the annealing temperature. Thus, the distribution of chromium in the test sample with an increase in temperature leads to the appearance of chromium nitride (Cr_2N), which was obtained on XRD patterns (Fig. 8).

Annealing of CL50WS powder in the inert nitrogen atmosphere

Figure 11 shows transmission Mössbauer spectra for CL50WS metallic powder annealed at the inert nitrogen atmosphere. As can be seen in the figure, at annealing

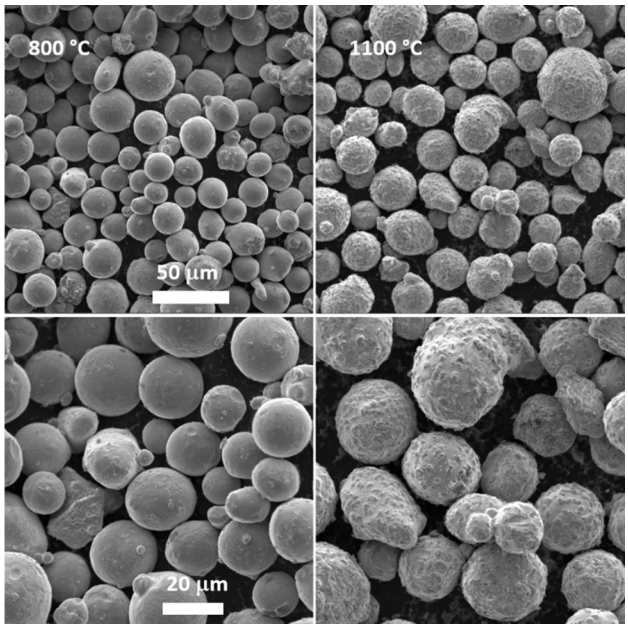

Fig. 9 Scanning electron microscopy images of annealed CL20ES powder in the inert nitrogen atmosphere

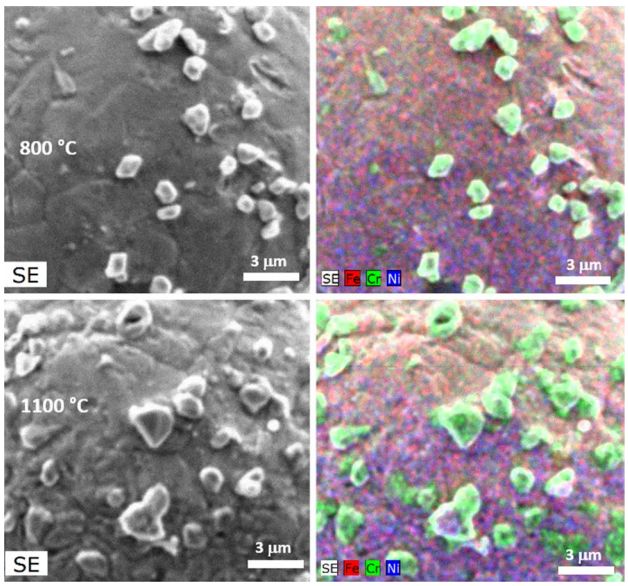

Fig. 10 Scanning electron microscopy images of the sphere surface of annealed CL20ES powder in the inert nitrogen atmosphere with the basic element mapping

temperatures from 500 to 800 °C, in addition to the austenitic phase of iron, there is also a ferritic phase. At an annealing temperature of 700 °C, the majority intensity on the spectrum falls on the austenitic phase, while the minority is related to the ferritic phase. The spectrum changes completely at the annealing temperature of 800 °C when the ferritic phase becomes the majority. At annealing in 900, 1000 and 1100 °C, the austenitic phase completely transforms into the ferritic. All hyperfine parameters are presented in Table 5. The ferritic phase is characterized by the distribution of hyperfine magnetic fields. The distribution of hyperfine magnetic fields narrows after annealing at temperatures of 500, 600 and 700 °C (Fig. 12). After annealing at higher temperatures, the distribution of hyperfine magnetic fields broadens, indicating a lower magnetic order of the system. All the results obtained with TMS are confirmed by XRD studies (Fig. 13).

The results of SEM for samples annealed at temperatures 500, 800 and 1100 °C are presented in Fig. 14. As can be seen, temperature annealing in an inert atmosphere does not lead to the sintering of the material and particles keep their original spherical shape. It can also be concluded that annealing of managing metal powders in the inert nitrogen atmosphere does not lead to the appearance of any nitrites on the surface of the particles.

Conclusions

The effect of annealing temperature and atmosphere on stainless (CL20ES) and maraging (CL50WS) steel powders was studied. Powders were annealed in the oxygen and inert nitrogen atmospheres in the temperature range from 500 to 1100 °C.

Stainless steel powder during annealing in the oxidizing atmosphere showed a tendency to the formation of iron oxides and the transformation of the austenitic phase of iron into the ferritic phase. Oxidation started at an annealing temperature of 700 °C and its intensity increased with increasing temperature. The product of oxidation at temperatures up to 900 °C was only α-Fe_2O_3. At a temperature of 1000 °C, the formation of Fe_3O_4 also began. At a temperature of 1100 °C, more FeO was added. The transformation of the austenitic to ferritic phase was observed at temperatures of 1000 and 1100 °C. Oxidation apparently took place on the surface of the spherical particles at temperatures up to 800 °C. Furthermore, as the temperature rises, the particles are destroyed. During the annealing of stainless steel powder in the inert nitrogen atmosphere up to annealing temperatures of 1000 °C, the austenitic phase remains. At a temperature of 1100 °C, a weak transformation of the austenitic to ferritic phase was observed. Annealing of stainless steel powder in a nitrogen atmosphere at temperatures of 900 °C and higher led to the diffusion of chromium to the surface of spherical particles to form Cr_2N. These particles with a size of approx. 1 µm occur separately on the surface of a spherical particle of stainless steel powder. Annealing the CL20ES powder did not lead to the destruction of the spherical particles or their sintering.

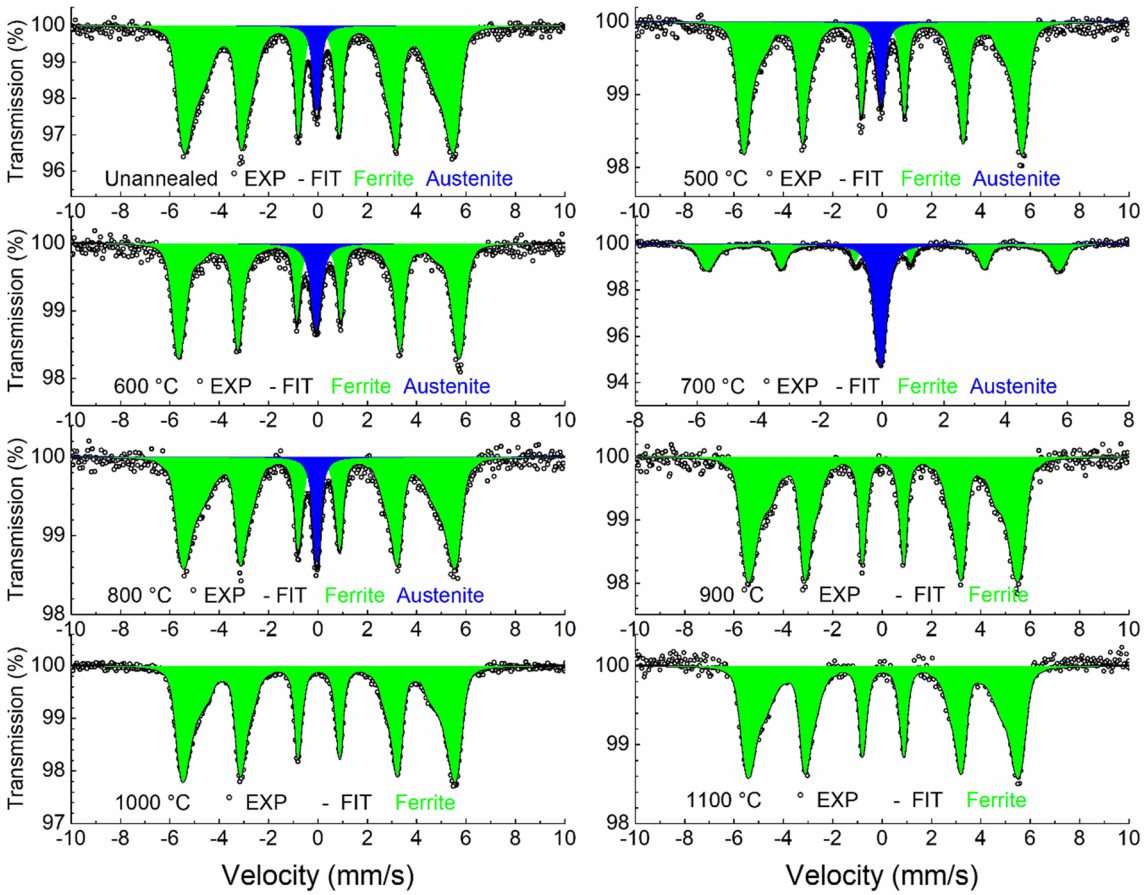

Fig. 11 Mössbauer spectra of annealed CL50WS powder in the inert nitrogen atmosphere

Table 5 Mössbauer parameters of annealed CL50WS powder in inert nitrogen atmosphere (IS—isomer shift, QS/ε—quadrupole splitting/shift, FWHM—full width at half maximum, B—hyperfine magnetic field, A—spectrum area)

Temperature	Phase	IS [mm/s]	QS [mm/s]	FWHM [mm/s]	B [T]	A [%]
Unannealed	FCC austenite	−0.06 ± 0.01	0.16 ± 0.02	0.34 ± 0.02	–	8 ± 1
	BCC ferrite	0.02 ± 0.01	–	0.27 ± 0.01	31.7*	92 ± 1
500 °C	FCC austenite	−0.05 ± 0.01	0.08 ± 0.02	0.37 ± 0.02	–	9 ± 1
	BCC ferrite	0.03 ± 0.01	–	0.25 ± 0.01	33.8*	91 ± 1
600 °C	FCC austenite	−0.07 ± 0.01	0.12 ± 0.5	0.44 ± 0.04	–	14 ± 1
	BCC ferrite	0.04 ± 0.01	–	0.25 ± 0.01	34.3*	86 ± 1
700 °C	FCC austenite	−0.05 ± 0.01	0.17 ± 0.02	0.36 ± 0.02	–	50 ± 1
	BCC ferrite	0.03 ± 0.01	–	0.24 ± 0.01	33.8*	50 ± 1
800 °C	FCC austenite	−0.06 ± 0.01	0.16 ± 0.02	0.28 ± 0.02	–	10 ± 1
	BCC ferrite	0.04 ± 0.01	–	0.24 ± 0.01	32.5*	90 ± 1
900 °C	BCC ferrite	0.04 ± 0.01	–	0.25 ± 0.02	32.6*	100
1000 °C	BCC ferrite	0.04 ± 0.01	–	0.25 ± 0.02	32.5*	100
1100 °C	BCC ferrite	0.05 ± 0.01	–	0.26 ± 0.02	32.7*	100

During the annealing of maraging steel (CL50WS) powder, the austenitic phase transformed to ferritic at temperatures greater than 800 °C. At lower annealing temperatures, the amount of austenitic phase was constant. Already at a temperature of 600 °C, the oxidation of the ferritic phase began, the intensity of which reached a maximum (almost complete oxidation) at a temperature of 900 °C. The oxidation products were α-Fe_2O_3 and Fe_3O_4. At temperatures of 1000 and 1100 °C, the oxidation was faster and an oxide shell was formed on the surface of the spherical particles,

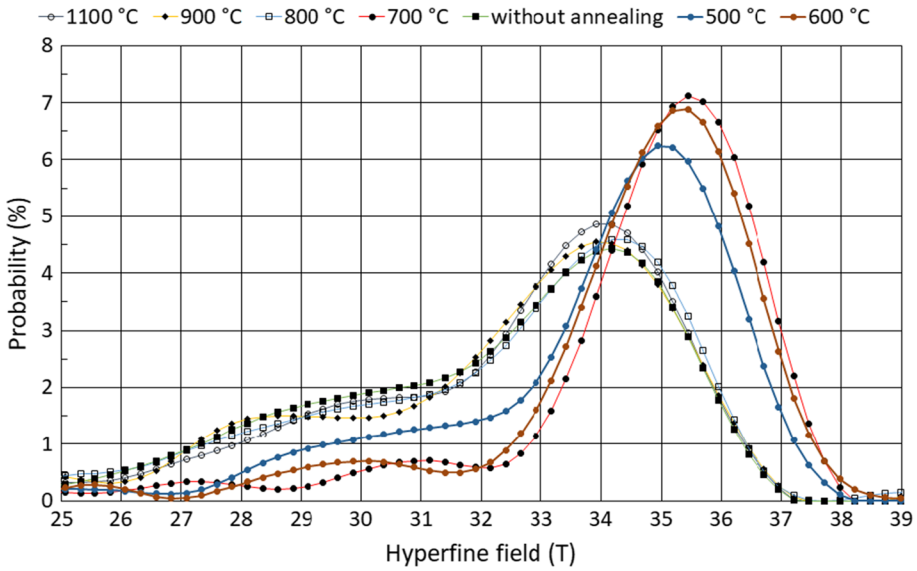

Fig. 12 The distribution of the hyperfine magnetic field

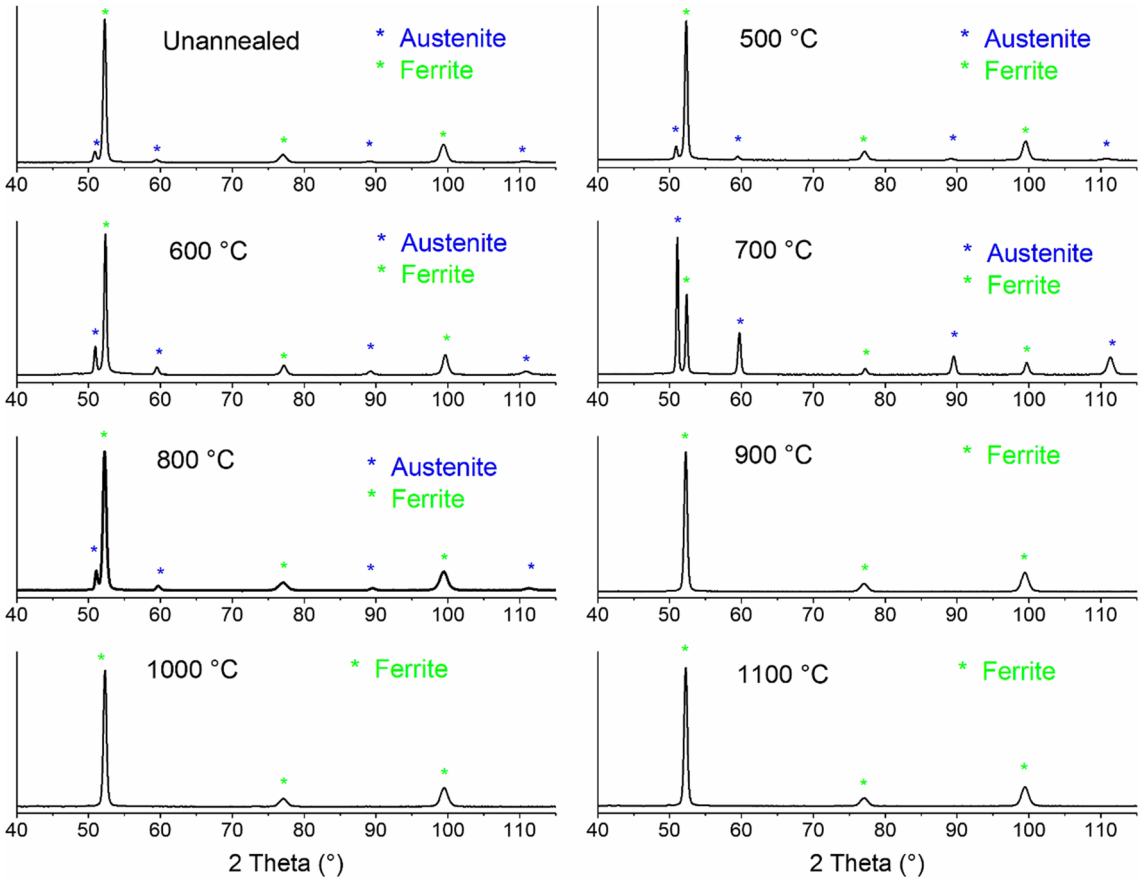

Fig. 13 X-ray diffraction patterns of annealed CL50WS powder in the inert nitrogen atmosphere

preventing the penetration of oxygen in depth. As a result of this oxidation, it was not complete and FeO and even a ferritic phase were observed in the samples. A spinel structure, probably close to $TiFe_2O_4$, was identified when maraging steel (CL50WS) powder was annealed. The oxidation process is accompanied by the destruction of spherical particles. During the annealing of CL50WS powder in a nitrogen atmosphere, an intensive transformation of the ferritic phase

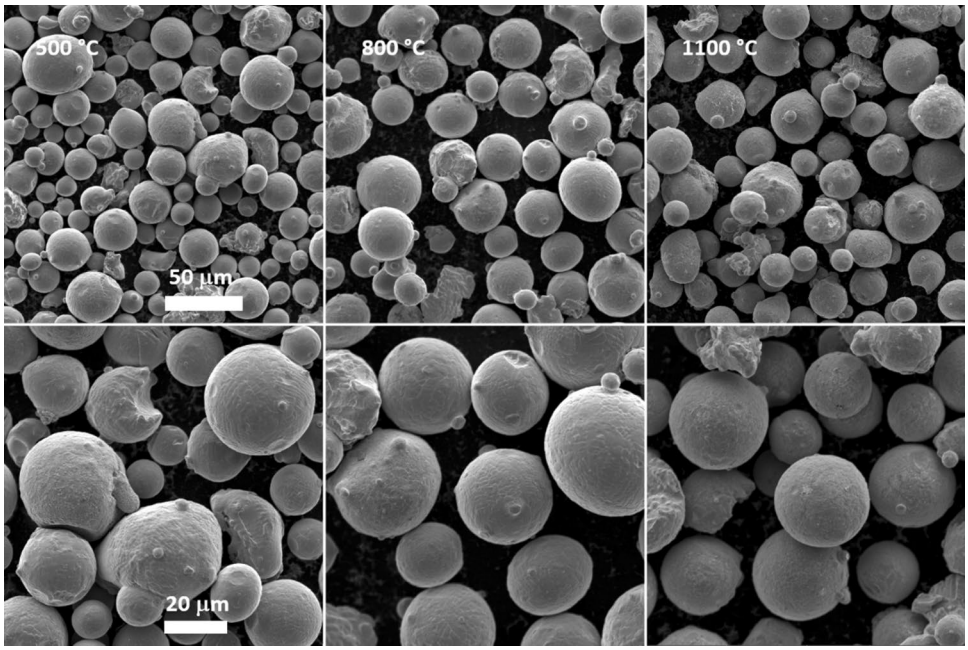

Fig. 14 SEM images of annealed CL50WS metal powder in the inert nitrogen atmosphere

to austenitic occurred at a temperature of around 700 °C. At annealing temperatures greater than 900 °C, the austenitic phase was fully transformed into ferritic. Annealing CL50WS powder did not lead to the destruction of spherical particles or their sintering.

Acknowledgements The authors thank the financial support by an internal IGA Grant of Palacký University (IGA_PrF_2023_003) and the Czech Ministry of Education, Youth and Sports, Grant Number CZ. 02.1.01/0.0/0.0/17_049/0008408.

Funding Open access publishing supported by the National Technical Library in Prague.

Declarations

Conflict of interest On behalf of all authors, the corresponding author states that there is no conflict of interest.

References

Ahlawat A, Sathe VG, Reddy VR, Gupta A (2011) Mossbauer, Raman and X-ray diffraction studies of superparamagnetic $NiFe_2O_4$ nanoparticles prepared by sol–gel auto-combustion method. J Magn Magn Mater 323:2049–2054. https://doi.org/10.1016/j.jmmm.2011.03.017

Barabaszová KČ, Slíva A, Kratošová G, Holešová S, Volodarskaja A, Cetinkaya T, Brožová S, Kozubek L, Martynková GS (2022) Phase transformation after heat treatment of Cr-Ni stainless steel powder for 3D printing. Materials 15:5343. https://doi.org/10.3390/ma15155343

Bautista A, Velasco F, Campos M, Rabanal ME, Torralba JM (2003) Oxidation behavior at 900 °C of austenitic, ferritic, and duplex stainless steels manufactured by powder metallurgy. Oxid Met 59:373–393. https://doi.org/10.1023/A:1023000329514

Chao Q, Thomas S, Birbilis N, Cizek P, Hodgson PD, Fabijanic D (2021) The effect of post-processing heat treatment on the microstructure, residual stress and mechanical properties of selective laser melted 316L stainless steel. Mater Sci Eng A 821:141611. https://doi.org/10.1016/j.msea.2021.141611

Chinnasamy CN, Narayanasamy A, Ponpandian N, Chattopadhyay K, Shinoda K, Jeyadevan B, Tohji K, Nakatsuka K (2001) Mixed spinel structure in nanocrystalline $NiFe_2O_4$. Phys Rev B 63:184108. https://doi.org/10.1103/PhysRevB.63.184108

Cook DC (1987) Strain induced martensite formation in stainless steel. Metall Mater Trans A Phys Metall Mater Sci 18:201–210. https://doi.org/10.1007/BF02825701

Cristobal AA, Aglietti EF, Porto Lopez JM, Sives FR, Mercader RC (2008) Mechanochemical activation of a titanium–magnetite mixture: Mössbauer spectroscopy study. J Eur Ceram Soc 28:2725–2730. https://doi.org/10.1016/j.jeurceramsoc.2008.03.034

Florez M, Ribas G, Cardoso J, Garcia A, Rovira J, Bastos-Neto M, Abreu H, Silva M (2021) Oxidation behavior of maraging 300 alloy exposed to nitrogen/water vapor atmosphere at 500°C. Metals 11:1021. https://doi.org/10.3390/met11071021

Fyodorov AA, Kholmetskii AL, Korzhik MV, Lopatik AR, Mashlan M, Misevich OM (1994) High performance transmission

Mössbauer spectroscopy with $YALO_3$: Ce scintillation detector. Nucl Instrum Meth Phys Res B 88:462–464. https://doi.org/10.1016/0168-583X(94)95398-8

Gerov MV, Kayasova AO, Kolmakov AG, Prosvirnin DV, Terentev VF (2022) Mechanical properties and fracture of high-strength maraging steel fabricated by selective laser melting. Russ Metall 4:309–315. https://doi.org/10.1134/S0036029522040139

Guan K, Wang ZM, Gao M, Li XY, Zeng XY (2013) Effects of processing parameters on tensile properties of selective laser melted 304 stainless steel. Mater Des 50:581–586. https://doi.org/10.1016/j.matdes.2013.03.056

Ivanova T, Mashlan M, Ingr T, Doláková H, Sarychev D, Sedláčková A (2022) Mössbauer spectroscopy for additive manufacturing by selective laser melting. Metals 12:551. https://doi.org/10.3390/met12040551

Kang N, Ma WY, Heraud L, El Mansori M, Li FH, Liu M, Liao HL (2018) Selective laser melting of tungsten carbide reinforced maraging steel composite. Addit Manuf 22:104–110. https://doi.org/10.1016/j.addma.2018.04.031

Klencsar Z, Kuzmann E, Vertes A (1996) User-friendly software for Mössbauer spectrum analysis. J Radioanal Nucl Chem 210:105–118. https://doi.org/10.1007/BF02055410

Klencsar Z, Kuzmann E, Vértes A (1998) User-friendly program for multifold evaluation of Mössbauer spectra. Hyperfine Interact 112:269–274. https://doi.org/10.1023/A:1010866928491

Kurikka VP, Shafi M, Gedanken A, Prozorov R, Balogh J (1998) Sonochemical preparation and size dependent properties of nanostructured $CoFe_2O_4$ particles. Chem Mater 10:3445–3450. https://doi.org/10.1021/cm980182k

Lei J, Ge Y, Liu T, Wei Z (2021) Effects of heat treatment on the microstructure and mechanical properties of selective laser melting 316L stainless steel. Shock Vib 2021:6547213. https://doi.org/10.1155/2021/6547213

Linderhof F, Mashlan M, Doláková H, Ingr T, Ivanova T (2021) Surface Micromorphology and structure of stainless and maraging steel obtained via selective laser melting: a Mössbauer spectroscopy study. Metals 11:1028. https://doi.org/10.3390/met11071028

Lu BH, Li DC, Tian XY (2015) Development trends in additive manufacturing and 3D printing. Engineering 1:85–89. https://doi.org/10.15302/J-ENG-2015012

Mashlan M, Linderhof F, Davidova M, Kubickova H, Zemtsova E (2019) Changes of phase composition of maraging steel 12709 during selective laser melting. Hyperfine Interact 241:1–8. https://doi.org/10.1007/s10751-019-1665-9

Mudarra Navarro AM, Gil Rebaza AV, Salcedo Rdríguez KL, Melo Quintero JJ, Rodríguez Torres CE, Weissmann M, Errico JA (2019) Structural, electronic, and magnetic properties and hyperfine interactions at the Fe sites of the spinel $TiFe_2O_4$. Ab Initio, XANES and Mössbauer study. J Phys Chem C 123:21694–21703. https://doi.org/10.1021/acs.jpcc.9b06550

Pechousek J, Mashlan M (2005) Mössbauer spectrometer as a virtual instrument in the PXI/Compact PCI modular system. Czech J Phys 55:853–863. https://doi.org/10.1007/s10582-005-0087-x

Riffard F, Buscail H, Rabaste F, Caudron E, Cueff R, Issartel C, Karimi N, Perrier S (2002) Manganese effect on isothermal high temperature oxidation behavior of AISI 304 stainless steel. Mat Scien Forum 595–598:1127–1134. https://doi.org/10.4028/www.scientific.net/MSF.595-598.1127

Roy A, Kumar S, Banerjee D, Ghose J (2000) Mössbauer studies on titanium substituted molybdenum ferrite. Solid State Commun 114:143–148. https://doi.org/10.1016/S0038-1098(00)00013-2

Saeidi K, Gao X, Lofaj F, Kvetková L, Shen ZJ (2015) Transformation of austenite to duplex austenite-ferrite assembly in annealed stainless steel 316L consolidated by laser melting. J Alloys Compd 633:463–469. https://doi.org/10.1016/j.jallcom.2015.01.249

Salman OO, Gammer C, Chaubey AK, Eckert J, Scudino S (2019) Effect of heat treatment on microstructure and mechanical properties of 316L steel synthesized by selective laser melting. Mater Sci Eng A 748:205–212. https://doi.org/10.1016/j.msea.2019.01.110

Sedláčková A, Ivanova T, Mashlan M, Doláková H (2022) Phase changes in the surface layer of stainless steel annealed at a temperature of 550 °C. Materials 15:8871. https://doi.org/10.3390/ma15248871

Wang L, Ding J, Roy A, Ghose J, Li Y, Feng YP (2000) Cluster-glass behaviour of the substituted molybdenum ferrite: a magnetic and Mössbauer study. J Phys Condens Matter 12:9963–9972. https://doi.org/10.1088/0953-8984/12/48/312

Yang JJ, Wang Y, Li FZ, Huang WP, Jing GY, Wang ZM, Zeng XY (2019) Weldability, microstructure and mechanical properties of laser-welded selective laser melted 304 stainless steel joints. J Mater Sci Technol 35:1817–1824. https://doi.org/10.1016/j.jmst.2019.04.017

Zboril R, Mashlan M, Petridis D (2002) Iron(III) oxides from thermal processes-synthesis, structural and magnetic properties, Mössbauer spectroscopy characterization, and applications. Chem Mater 14:969–982. https://doi.org/10.1021/cm0111074

Zeng Q, Gan K, Wang Y (2021) Effect of heat treatment on microstructures and mechanical behaviors of 316L stainless steels synthesized by selective laser melting. J Mater Eng Perform 30:409–422. https://doi.org/10.1007/s11665-020-05330-7

Zhou Z, Wang S, Li J, Li Y, Wu X, Zhu Y (2020) Hardening after annealing in nanostructured 316L stainless steel. Nano Mater Sci 2:80–82. https://doi.org/10.1016/j.nanoms.2019.12.003